


A laboratory spectrometer for high throughput X-ray emission spectroscopy in catalysis research

Cite as: Rev. Sci. Instrum. **89**, 113111 (2018); <https://doi.org/10.1063/1.5035171>

Submitted: 13 April 2018 . Accepted: 24 October 2018 . Published Online: 15 November 2018

Wolfgang Malzer, Daniel Grötzsch, Richard Gnewkow, Christopher Schlesiger, Fabian Kowalewski, Benjamin Van Kuiken , Serena DeBeer, and Birgit Kanngießer



View Online



Export Citation



CrossMark

ARTICLES YOU MAY BE INTERESTED IN

[A novel von Hamos spectrometer for efficient X-ray emission spectroscopy in the laboratory](#)

Review of Scientific Instruments **85**, 053110 (2014); <https://doi.org/10.1063/1.4875986>

[An improved laboratory-based x-ray absorption fine structure and x-ray emission spectrometer for analytical applications in materials chemistry research](#)

Review of Scientific Instruments **90**, 024106 (2019); <https://doi.org/10.1063/1.5049383>

[A laboratory-based hard x-ray monochromator for high-resolution x-ray emission spectroscopy and x-ray absorption near edge structure measurements](#)

Review of Scientific Instruments **85**, 113906 (2014); <https://doi.org/10.1063/1.4901599>



JANIS

Rising LHe costs? Janis has a solution.
Janis' Recirculating Cryocooler eliminates the use of Liquid Helium for "wet" cryogenic systems.

sales@janis.com www.janis.com [Click for more information.](#)

A laboratory spectrometer for high throughput X-ray emission spectroscopy in catalysis research

Wolfgang Malzer,¹ Daniel Grötzsch,¹ Richard Gnewkow,¹ Christopher Schlesiger,¹ Fabian Kowalewski,² Benjamin Van Kuiken,² Serena DeBeer,² and Birgit Kanngießer¹

¹*Institute for Optic and Atomic Physics, Technische Universität Berlin, Hardenbergstr. 36, 10623 Berlin, Germany*

²*Max Planck Institute for Chemical Energy Conversion, Stiftstr. 34-36, 45470 Mülheim an der Ruhr, Germany*

(Received 13 April 2018; accepted 24 October 2018; published online 15 November 2018)

We have built a laboratory spectrometer for X-ray emission spectroscopy. The instrument is employed in catalysis research. The key component is a von Hamos full cylinder optic with Highly Annealed Pyrolytic Graphite (HAPG) as a dispersive element. With this very efficient optic, the spectrometer subtends an effective solid angle of detection of around 1 msr, allowing for the analysis of dilute samples. The resolving power of the spectrometer is approximately $E/\Delta E = 4000$, with an energy range of ~ 2.3 keV–10 keV. The instrument and its characteristics are described herein. Further, a comparison with a prototype spectrometer, based on the same principle, shows the substantial improvement in the spectral resolution and energy range for the present setup. The paper concludes with a discussion of sample handling. A compilation of HAPG fundamentals and related publications are given in a brief Appendix. *Published by AIP Publishing.* <https://doi.org/10.1063/1.5035171>

INTRODUCTION

In X-ray emission spectroscopy (XES), X-ray line spectra are measured with a spectral resolution sufficient to analyze the impact of the chemical environment on the X-ray line energy and on branching ratios. To our knowledge, the first XES experiments were published by Lindh and Lundquist in 1924.¹ In these early studies, the authors utilized the electron beam of an X-ray tube to excite core electrons and obtain the $K\beta$ line spectra of sulfur and other elements. Three years later, Coster and Druyvesteyn performed the first experiments using photon excitation.² Their work demonstrated that the electron beams produce artifacts,² thus motivating the use of X-ray photons for creating the core hole. Subsequent experiments were carried out with commercial X-ray spectrometers,³ as well as with high-resolution spectrometers.⁴ While these early studies provided fundamental insights into the electronic configuration of small molecules, XES only came into broader use with the availability of high intensity X-ray beams at synchrotron radiation facilities, which enabled the measurement of (chemically) dilute samples.⁵ In addition to the experimental advances, it is also the progress in quantum chemical computations, which makes XES an intriguing tool for the study of the electronic structure of chemical compounds.^{6,7}

While synchrotron radiation experiments provide a unique sensitivity and flexibility, the access to it is limited. The motivation of this work is to overcome this limitation and to better exploit the potential XES offers for research in chemistry. The goal was to build a laboratory based spectrometer, which is capable of high-throughput XES analysis of samples that are relevant in catalysis research.

During the last decade, various X-ray analyzers for synchrotron applications were built. In order to preserve high resolving power and to increase the solid angle of detection, multi-crystal analyzer setups were developed. These include setups based on the Johann geometry, which were built by

Sokaras *et al.*⁸ and Kleymenov *et al.*,⁹ as well as von Hamos type setups built by Hayashi *et al.*¹⁰ and Alonso-Mori *et al.*¹¹ In addition, laboratory spectrometers for XES, which are based on spherically bent crystals, were developed by Seidler *et al.*¹² and Holden *et al.*¹³

The XES spectrometer, which is presented in this paper, is based on the developments published previously by Anklamm *et al.*¹⁴ As an X-ray tube is used for excitation, which is much less brilliant than synchrotron radiation, the analyzer part of the spectrometer must be extremely efficient to allow for the detection of the weak valence-to-core lines even in dilute samples.

The laboratory XES spectrometer is based on the von Hamos principle, and the entire spectrum is taken without moving any spectrometer components. In order to achieve the high efficiency required for XES with laboratory sources, a full 360° collection geometry is utilized. The X-ray lines are mapped as rings onto the CCD, which is used as a position sensitive detector. To further maximize the sensitivity, a mosaic crystal with high integral reflectivity, Highly Annealed Pyrolytic Graphite (HAPG), was used as a dispersive element. The effective solid angle of such a ring optic has a magnitude of around 1 msr.

The first setup we developed used a 100 W X-ray tube with a poly-capillary concentrator for the excitation of the sample and an X-ray CCD for detection. The spectral resolving power, we achieved with the prototype setup, was approximately $E/\Delta E = 2000$, and the effective solid angle (reflectivity \times solid angle) covered by the analyzer optic is in the range of a few msr. The instrument is capable of measuring good quality XES spectra on dilute samples over a period of several hours.

In comparison with this first setup, major improvements could be achieved. The spectral resolving power of the instrument presented in this paper could be increased significantly from $E/\Delta E = 2000$ to $E/\Delta E = 4000$. The loss in the effective solid angle of detection connected with the higher resolving

power was compensated by a more powerful excitation through a Ga-jet X-ray source. The range of elements, which can be analyzed, was also extended. The first setup was capable of measuring the K-lines of elements with atomic numbers higher than Ca. With the new setup, it is possible to measure the K-lines of sulfur-containing compounds.

OVERVIEW OF THE INSTRUMENT

Figure 1 shows a graphical view of the XES spectrometer. The large vacuum vessel on the right side houses the X-ray analyzer. The ring optic and the X-ray CCD are mounted on a 3.5 m long rail system. At the largest distance possible, the Zn K β lines at \sim 9.5 keV can be measured in the first order of reflection. With the ring and the CCD positioned as close to the sample as possible, sulfur emission lines at 2.3 keV can be measured.

The sample is excited by a Ga-jet X-ray source manufactured by Excillum (www.excillum.com), which is operated at a power of 250 W. As the diameter of the analyzer housing is 800 mm, the radiation has to be transferred over a distance of almost 500 mm from the X-ray source to the sample. This is achieved with a polycapillary X-ray lens manufactured by the Institute for Scientific Instruments (IFG, www.ifg-adlershof.de). The X-rays are concentrated onto a spot of \sim 30 μ m in diameter. The FWHM of the focal spot was measured by a knife edge scan. The intensity gain, determined as the ratio of count rates measured through a pinhole of 10 μ m diameter, is specified by the manufacturer to be slightly above 20 000 within the energy range of 5 keV–20 keV.

A directly detecting deep depletion back illuminated X-ray CCD (Princeton Instruments) serves as a detector. The detector area is 1 in. \times 1 in. with 1300 \times 1340 20 μ m pixels.

The samples are loaded into the instrument through the glove box on the left side. Inside the glove box, they are fixed onto the sample holder. A bayonet clutch serves as the mount for the sample holder to the finger of the cryo-cooling unit (Advanced Research Systems, Cryoandmore). After the

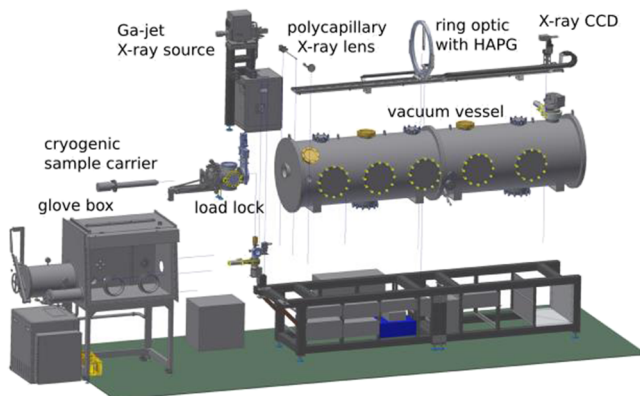


FIG. 1. Schematic view of the XES spectrometer. On the right hand-side, the ring, which is coated with the HAPG crystal, is displayed. Together with the CCD, it is mounted on a rail system which allows Bragg angles to be selected for an energy range of 2.3 keV–10 keV. The load lock can be separated by a valve from the analyzer vessel. As the load lock is inside the glove box, sample handling without exposure to oxygen or humidity is possible.

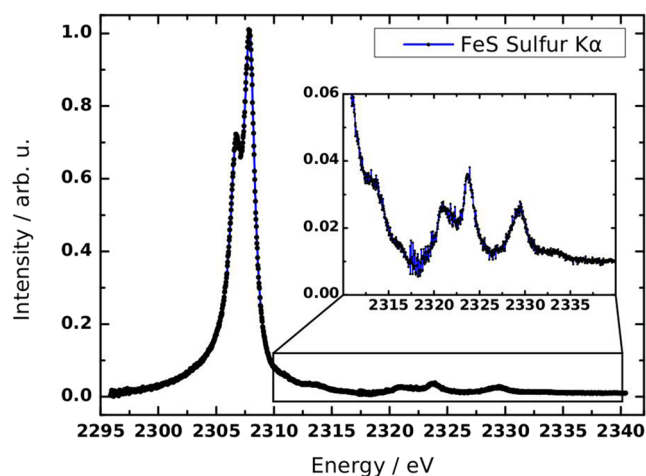


FIG. 2. K α spectrum of sulfur. The S K α spectrum of FeS was taken in two steps as the energy bandwidth at 2300 eV is 20 eV. The measurements took 1 h for the main lines and 5 h for the satellite lines above 2317 eV.

vacuum load lock is evacuated, the sample can be transferred to the main vacuum chamber and moved into the focus of the polycapillary X-ray lens.

By performing the measurements in vacuum, the accessible energy range of the present instrument is greatly extended relative to that of Anklamm *et al.* The prototype setup has an entrance window, which separates the sample, measured in air, from the analyzer operated in vacuum. While the crystal and the detector can be positioned for energies down to 2.5 keV, the entrance window increasingly masks parts of the crystal ring beginning at the Ca K-alpha lines. In combination with absorption due to the entrance window, the spectrometer's sensitivity drops off drastically toward lower energies and renders it useless below \sim 4 keV.

By contrast, with the sample in the same vacuum vessel as the analyzer, the measurement of emission lines down to the sulfur K-alpha lines is feasible. Figure 2 depicts an S K α spectrum of FeS. The measurement was carried out in two steps with 1 h for the main lines and 5 h for the satellite lines in the energy range from 2317 eV to 2326 eV.

SPECTROMETER CHARACTERISTICS

A major design goal of the present spectrometer development was to increase the spectral resolving power relative to the previous instrument. For this reason, the geometry of the ring was modified. Namely, its diameter was doubled, from 300 mm to 600 mm, and the thickness of the HAPG crystal layer was halved from 40 μ m to 20 μ m. An optic of this size presents a real manufacturing challenge as the mold must consist of glass and the surface must be polished to optical quality without introducing shape errors. If these conditions were both met, the mosaic spread of the HAPG would not be as low as required. In a cooperation of the optic manufacturer Optigraph (www.optigraph.eu) and TU Berlin, the mold for the ring optic could be manufactured in one piece.

Besides the thickness of the crystal, its mosaic spread is crucial for a high resolving power and low peak tailing. We determined the mosaic spread of the HAPG crystal in

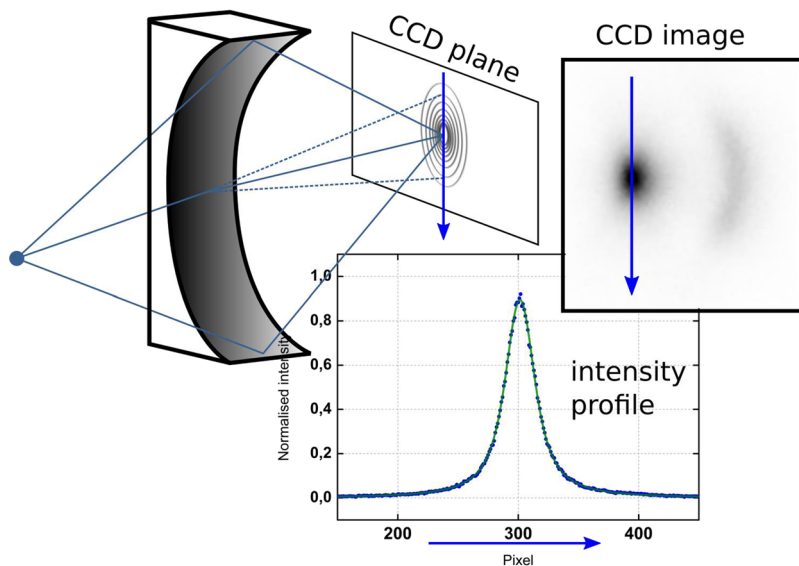


FIG. 3. Determination of the mosaic spread. The figure outlines the determination of the mosaic spread following Jarrott *et al.*¹⁷ For the characterization of the mosaic spread, only 20° of the crystal ring is illuminated. A customized sample holder is used to block the remaining 340° of the optic. The CCD is positioned at the focal point of the emission line, which is used for the measurement. The image of this line is extended toward the direction of dispersion and perpendicular to it. The broadening perpendicular to the direction of dispersion is mainly due to the mosaic distribution of the crystallites. They reflect X-rays within a small segment of a cone, indicated by dotted lines.

18 sections of 20° each. For that purpose, we used an Fe-target inside a customized sample holder. This holder shielded most of the ring optic, allowing for the irradiation of only 20° sections of the optic. The setup for this measurement resembles the standard von Hamos geometry. The X-ray CCD was positioned in the focal plane of the Fe $K\alpha_1$ line.

Figure 3 illustrates the principle of the measurement, which was also used by Jarrott *et al.*¹⁷ The CCD image of the X-ray line shows broadening not only in the direction of dispersion but also perpendicularly to it in the sagittal direction. The sagittal profile is dominated by a contribution from the finite source size and an additional broadening, which is directly caused by the mosaic profile. Therefore, the mosaic spread can be determined from the sagittal profile of X-ray emission lines. The mosaic spread of the crystal was determined to be 0.06° , which is the optimum achievable according to our experience.

Based on the measurement of the mosaicity, the source size ($30 \mu\text{m}$), the pixel size of the detector ($20 \mu\text{m}$), and an intrinsic broadening of 14 arc sec,¹⁵ we determined the spectral resolving power. The result of the calculation is shown in Fig. 4 together with the result of an experimental determination, which followed the procedure described by Anklam.^{14,16}

The spectral broadening of this spectrometer is dominated by the intrinsic broadening of the crystal. Thus, the spectral resolving power is close to the maximum achievable. At this point, we also note that the actual resolution strongly depends on the sample preparation. In certain cases, the thickness of the sample may dominate the resolution, as is discussed in detail later in this report. The resolution also varies with the ring position on the detector, as shown in a previous paper by Anklam *et al.*¹⁴

Experimentally determined values and calculated values deviate by up to 5% from each other. As mentioned above, the variation of attenuation length affects the actual source size and thus the spectral resolution. The estimate of the resolution does not take into account these variations. Further, errors of literature data for the core hole lifetime broadening and the simplified X-ray line model consisting of only the two major

lines $K\alpha_1$ and $K\alpha_2$ add to the uncertainty of the experimentally determined spectral broadening.

A comparison of spectra taken with the first setup and the new one demonstrates the improvement (Fig. 5). We note that both the resolving power (in terms of FWHM of the peaks) and also the tailing are reduced strikingly. As discussed in detail in Anklam *et al.*,¹⁴ one of the consequences of the crystal mosaicity is an asymmetric peak profile. The previous HAPG ring optic shows a pronounced tailing on one side, which hampers the evaluation of weak emission lines located next to strong ones. The reduction in the mosaic spread from previously 0.1° to 0.06° reduces the tailing, and the $K\beta'$ in the FeS spectrum shown in the right panel of Fig. 5 is clearly better resolved from the main line as compared to the measurements obtained with the prototype instrument.

As a consequence of optimizing the resolving power, the optic's effective solid angle of detection is lower than that of the

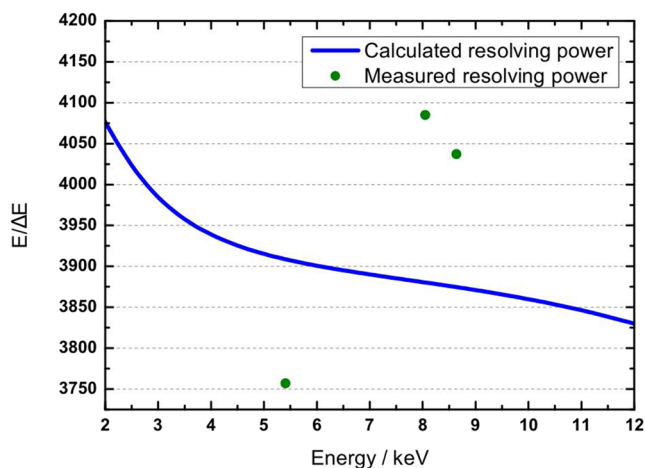


FIG. 4. Resolving power. The resolving power of the XES spectrometer is approximately $E/\Delta E = 4000$ over the entire range of energy. The calculated values include the broadening by the mosaic crystal, by the source size and by the pixel size of the detector. Measured resolving powers were determined using metal foils. Dilute samples may show noticeable penetration effects, which worsen the spectral resolution.

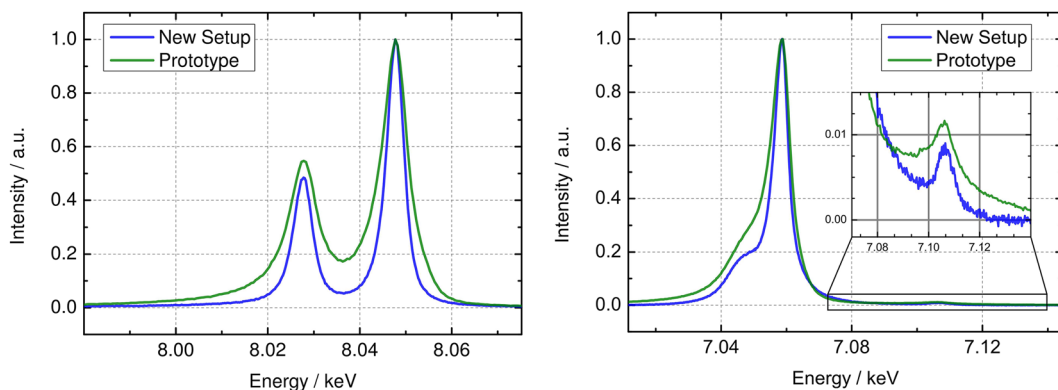


FIG. 5. Comparison between the current setup and the prototype setup reported in Ref. 4. The graph on the left-side demonstrates the improved resolving power and the reduction in the peak tailing by a comparison of Cu K α spectra. This improvement is also obvious in the example shown on the right-side, which depicts the K β multiplet of FeS. The K- β' line at the low energy side of the main line is much better resolved.

first setup. The main reason is the lower thickness of the crystal layer, which reduces the integral reflectivity by approximately a factor of two. Figure 6 compares the effective solid angle of detection for both optics. We note that the effective solid angle of the ring optic is reported as the product of the solid angle subtended and the integral reflectivity of the crystal.

This loss in the solid angle of detection is more than compensated by the use of a more powerful X-ray source. We used a Ga-jet X-ray source, which is operated at 250 W. The advantages of the Ga-Jet source include the high brilliance, as well as the use of Ga as a target, which characteristic radiation excites first row transition metals up to Cu, and even Zn with Ga K β . The radiation is transferred to the target by using a 500 mm long polycapillary X-ray lens with a focal spot size of around 30 μ m.

The energy band width of the instrument depends on the meridional length of the crystal and on the size of the detector.

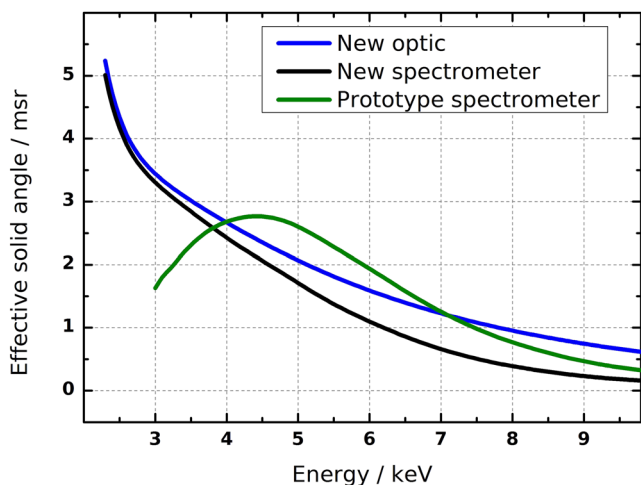


FIG. 6. Effective solid angle of the optic and spectrometer. The plot compares the effective solid angle for the center energy of the prototype spectrometer with the new one. For the new spectrometer, the effective solid angle of the optic is shown. It represents the optics capability to reflect photons emitted by the source onto the detector. The effective solid angle of the entire spectrometer additionally takes into account the detector's quantum efficiency. The effective solid angle of the prototype spectrometer is larger because the crystal is 40 μ m thick in comparison with 20 μ m for the new one. Below 5 keV, its effective solid angle decreases due to absorption in the entrance window.

Figure 7 depicts both limits. In the energy range from 2.3 keV to 6 keV, the size of the X-ray CCD restricts the energy range, which increases linearly from \sim 20 eV to \sim 110 eV. Above 6 keV, the crystal length confines the bandwidth, which only slightly increases to \sim 125 eV at 10 keV.

CCD IMAGE EVALUATION

The X-ray emission lines appear as rings on the CCD, as shown in Fig. 8. The left image displays the Cu K-lines of metallic copper, the K α_1 at 8046.3 eV, and the weaker K α_2 at 8026.7 eV. The right image shows the two Cl K α -lines for KCl at 2622 eV and 2620 eV, respectively. While the Cu-lines produce well-shaped homogeneous rings, the Cl-rings are severely distorted. These distortions are an implication of the large take off aperture of ca. 90°. The incidence angle of the beam toward the sample surface must be shallow, and its actual footprint is around 5 times larger in the plane of beam and spectrometer axis compared to the vertical axis. The result

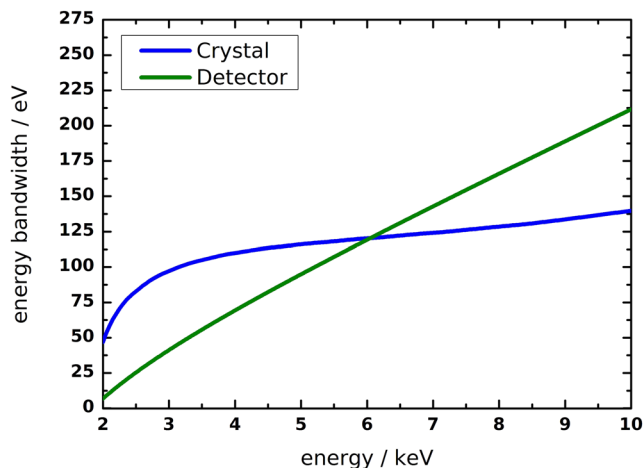


FIG. 7. Energy bandwidth. The bandwidth limit imposed by the size of the detector (1 in. \times 1 in.) is plotted in green. The bandwidth restriction due to meridional length of the crystal (20 mm) is shown by the blue line. In the energy range between 2.3 keV and 6 keV, the bandwidth is limited by the size of the detector. Above 6 keV, the crystal length confines the energy range.

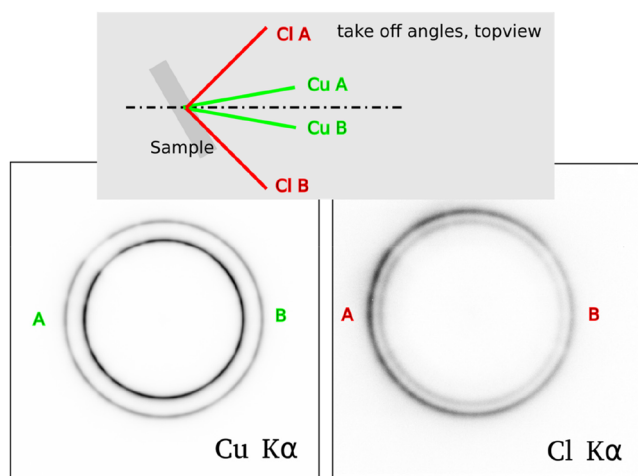


FIG. 8. CCD image of Cu and Cl $K\alpha$ lines. The chlorine spectrum of KCl was taken in a pre-focus geometry, where the radius of the ring increases with increasing energy. The copper spectrum was measured in a post-focus geometry, where this relation is inverted (see the work of Anklamm *et al.*¹⁴ for details). The weaker intensity at 11 o'clock, which the two spectra have in common, is due to a HAPG segment with slightly lower reflectivity. In comparison with the otherwise perfect circles of the X-ray image for the $K\alpha$ lines of metallic copper in the left panel, the intensity image for chlorine shows self-absorption effects. With the larger take off cone (indicated in red), the take off angle considerably varies, and the effects of self-absorption become severe. This asymmetry required a revision of the image evaluation as described in the respective section.

is the broadening of the ring in that plane. At the same time, the take off angle varies between an almost grazing angle on one side and almost perpendicular on the other side, causing a considerable difference in the count rate. These distortions made the automated CCD image evaluation as described below fail.

The CCD image evaluation consists of three steps: determine the center of the rings, sum the events along radius channels, and convert the radius channels to energy channels.⁴ The first step failed for the evaluation of measurements in the low energy range (e.g., S and Cl XES). The center of the ring was determined by a fit with a circle using the most intense pixels, but the strong asymmetries caused the center to be completely off. The procedure we follow now is more complex. For a given center, the spectrum is determined. The FWHM of the most intense peak is used as the criterion for the optimization. This new procedure is robust and reliable.

Further, the event detection was improved. To increase the signal to noise ratio for dilute samples, the CCD is operated in the single photon counting mode. When an X-ray photon is absorbed in the wafer of the detector, electron-hole pairs are created. The amount of charge created is proportional to the energy of the interacting photon. This allows energy discrimination with a CCD and can be used to suppress dark and readout noise, as well as events caused by higher order contributions or background radiation.

Depending on the pixel and charge cloud size, the total charge created by a single photon event can spread over multiple pixels. We improved the event detection for these split events using a pixel clustering approach with a spectral resolution of around 190 eV for Fe $K\alpha$. We added a detection of pile-up events, which now are attributed to the X-ray lines

under investigation. These improvements increased the yield of registered photons to almost 100%.

SAMPLE PREPARATION AND EXPERIMENTAL PRACTICE

One of the research approaches, which the XES spectrometer is used for, is comparisons of the spectra of series of compounds where the chemical environment of the element investigated is altered systematically and purposefully. The precision of the energy scale is crucial for this type of investigation.

The relation between photon energy and the ring on the detector depends on the Bragg angle, the radius of the X-ray optic, and the distance between source and the center of the ring image on the detector. The respective equation is given in Anklamm *et al.*¹⁴ In an initial energy calibration, the distance between the source and the detector is determined by means of a reference sample with known emission line energies. The spectrometer can be tuned to any energy with mechanical precision. As shown subsequently, the best precision requires the use of a reference sample before the analysis of unknown samples. The spectrometer allows a temporary redefinition of the source to sample distance.

As outlined above, the energy of an X-ray line is related to the diameter of its image on the CCD, and the distance between the source and the CCD is the critical property for the precision of the energy scale. Sample misalignment perpendicular to the optical axis of the spectrometer is much less critical. We investigate the stability and precision of the spectrometer energy scale for three modes of operation. First, for comparisons, where only the sample is changed and neither the CCD nor the crystal is moved between measurements. We aligned the test samples 10 times each and determined the standard deviation of the peak positions. For sample alignment, the center of the ring on the CCD is determined with a short measurement after bringing the sample into the beam. As the coordinates of the ring center for an aligned sample are known from the calibration, the deviation can be compensated. In most cases, the sample is aligned correctly after one step.

Second, we moved the CCD, which sometimes is useful, because one can inspect neighboring energy ranges. As the positioning of the CCD stage will dominate the uncertainty, the sample was not re-aligned for each of the measurements.

Finally, the energy scale was not determined by a reference measurement, but the spectrometer was simply set to the energy according to the initial energy calibration. CCD and crystal were moved between the test measurements in order to evaluate the reproducibility of motor movements as a possible source of error.

For the first mode of operation, the peak position had a standard deviation of around 20 meV for Cu, Cr, and K. We, however, note that this precision cannot be simply assumed for any experiment. Changing the model for peak fitting typically results in variations in the resulting line energies, which may be larger than the instrumental variations. The asymmetric spectrometer response hampers spectrum fitting. If we compare different substances, the uncertainty of line energies

will be higher than the deviations we obtained by the repeated measurement of the same substance.

The standard deviation for the second mode of measurement, the CCD was moved in between, ranges from 40 meV to 80 meV.

If the spectrometer is just moved to a new energy without recalibration with a reference measurement, the energy scale is shifted up to 1 eV. The precision for moving all spectrometer components has a standard deviation of 150 meV.

A final important practical consideration is the nature of the sample itself. For powder samples, hard X-ray measurements are commonly carried out by filling a metal spacer with sample powder and sealing it with transparent tape. Typical sample thicknesses are on the order of ~ 1 mm. For our instrument, the thickness of a dilute sample has a pronounced effect on the measurement resolution. This is due to the fact that a true sample is not a point source. Hence, photons emitted from the front and the back of the sample yield different distances between the source and the optic and are thus imaged at different points on the detector. In order to investigate the effects of sample thickness, a series of iron oxide (Fe_2O_3) samples was prepared with increasing dilution in BN. All samples were packed in 1 mm sample holders and measured at an angle of 45° with respect to the incident beam. Figure 9(a) shows Fe $K\alpha_1$ for the series of Fe oxide samples, and Table I compares the attenuation length for each sample with the FWHM of the $K\alpha_1$ and the count rate at the maximum of the $K\alpha_1$. Clearly there is a strong dependence of the spectral width on the attenuation length since the FWHM of the $K\alpha_1$ nearly doubles as the attenuation length increases from 9 to 606 μm .

The dependency of the spectral width on the attenuation length is potentially problematic when the sample is inherently dilute. For example, one may be interested in series of catalysts where a dopant appears in different concentrations. This could result in varying spectral widths and complicate the interpretation of the underlying chemistry. There are several possible

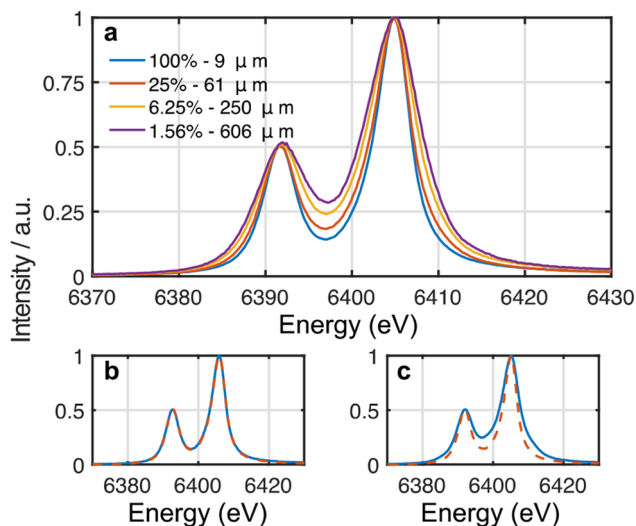


FIG. 9. Impact of sample characteristics on XES resolution. The dependence of the Fe $K\alpha_{1,2}$ spectrum of Fe_2O_3 when diluted in increasing amounts of BN (a). Mass percents of Fe_2O_3 and the attenuation length of the X-ray beam determined from atomic scattering factors are listed. Comparison of thick (blue line) and thin (dashed red line) samples for Fe_2O_3 (b) and $\text{Fe}(\text{TPP})$ (c).

TABLE I. Dependence of sample concentration on attenuation length, spectral width, and count rate.

Sample	Attenuation length (μm)	FWHM of $K\alpha_1$ (eV)	Count rate ($10^6/\text{s}$)
100% Fe_2O_3	9	4.83	2.5
25% $\text{Fe}_2\text{O}_3:\text{BN}$	61	5.47	1.5
6.25% $\text{Fe}_2\text{O}_3:\text{BN}$	250	6.83	0.66
1.56% $\text{Fe}_2\text{O}_3:\text{BN}$	606	7.87	0.21
$\text{Fe}(\text{TPP})$... ^a	6.26	0.56
Thin Fe_2O_3	...	4.73	0.55
Thin $\text{Fe}(\text{TPP})$...	4.52	0.01

^aDespite being a pure complex, the density of $\text{Fe}(\text{TPP})$ is not easily determined.

corrections for this issue. First, one could dilute all samples to obtain samples of equal concentration. This would result in comparable albeit broadened spectra. Second, thin samples can be employed. Figures 9(b) and 9(c) compare the results of using “thick” and “thin” samples in Fe_2O_3 and an inherently dilute sample, an iron tetraphenyl porphyrin, denoted $\text{Fe}(\text{TPP})$, respectively. Thin samples were prepared by spreading a thin layer of the sample powder on Kapton tape. In the case of Fe_2O_3 , the thick and thin samples are nearly identical, indicating that no substantial decrease in resolution is incurred for concentrated samples such as transition metal oxides. On the other hand, the dilute molecular sample shows a significant difference. The 1 mm thick sample of $\text{Fe}(\text{TPP})$ has a $K\alpha_1$ line width of 6.26 eV, but the thin sample exhibits a 4.52 eV width. Thus, the $\text{Fe}(\text{TPP})$ examples show a route for recovering the maximum instrument resolution for dilute systems through thoughtful sample preparation.

While preparing thin samples assures that one obtains the highest possible experimental resolution, thinner samples also result in decreased count rates. For a pure Fe_2O_3 , one achieves 2×10^6 counts per second (cps) at the maximum of the $K\alpha_1$. For dilute samples of iron oxide and for molecular complexes with large ligand systems, the count rate is an order of magnitude less. Similarly, there is about an order of magnitude decrease in going from a thick sample to a thin sample in the systems we have examined. For all samples, virtually noiseless $K\alpha$ lines can be obtained relatively quickly. On the other hand, if $K\beta$ valence-to-core spectra are desired, the counts are predicted to be reduced by a factor of 10^3 relative to the $K\alpha_1$ line. Consequently, there is a trade-off between the spectral resolution provided by thin samples and number of counts provided by thick concentrated samples. As a matter of practicality, measuring only powder spread on tape is not feasible for $K\beta$ VtC measurements due to the low counts. For example, the spectrum of $\text{Fe}(\text{TPP})$ spread on tape shows no well-resolved VtC feature after 7 h.

In summary, sample preparation must balance feasibility and spectral resolution, and the specific sample preparation strategy will depend on the chemical system of interest. Many heterogeneous catalysts are based on relatively simple concentrated complexes, such as transition metal oxides. Both thick and thin samples are likely suitable due to high signal levels and short X-ray attenuation lengths. For more dilute samples, such as molecular homogeneous catalysts, optimal sample conditions must be chosen balanced between the resolution

and signal level, and this will be performed on a case-by-case basis.

CONCLUSIONS

A spectrometer for X-ray emission spectroscopy measurements in the laboratory was built and characterized. Sample handling in an inert N₂-atmosphere and optional cryogenic cooling facilitate the analysis of reactive chemical compounds. Its high sensitivity enables experiments with dilute samples with acquisition times of typically 5–10 h.

In comparison with the prototype instrument, the current yields much higher quality of the XES spectra. The spectral resolving power is now $E/\Delta E = 4000$ instead of $E/\Delta E = 2000$. In addition, the peak tailing was reduced significantly. The second important progress is the extended range of elements, which can be analyzed. Spectra of sulfur compounds can be acquired, whereas the lightest element accessible with the first setup was calcium. In particular for dilute specimen, sample preparation is crucial in order to optimally utilize the laboratory XES-spectrometer's capabilities.

ACKNOWLEDGMENTS

S.D. acknowledges the Max Planck Society for funding. The development of the spectrometer was funded by the European Research Council under the European Union's Seventh Framework Programme (No. FP/2007-2013) ERC Grant Agreement No. 615414.

APPENDIX: FUNDAMENTALS OF HAPG OPTICS

Highly Oriented Pyrolytic Graphite (HOPG) is a kind of a niche material with respect to X-ray optics. By discussions and also thanks to the review process of this paper, we were made aware that knowledge on this material and on the fundamentals of optics made from mosaic crystals is not as widespread as for ideal crystals. To spare the interested reader the burden to search for that knowledge which is scattered in the literature of three decades, we compiled this short summary. It answers frequently asked questions and provides references to a selection of publications.

Properties of HOPG and HAPG

HOPG is a mosaic crystal, which consists of small crystallites of graphite with a thickness of ca. 1 μm . A breakthrough for the fabrication of X-ray optics was the development of flexible HOPG by Antonov and Grigorieva in the beginning of the 90s.¹⁸ Sheets of flexible HOPG with a thickness down to ca. 10 μm ¹⁹ can be mounted on substrates at room temperature. A review on its properties and application in X-ray spectroscopy can be found in Ref. 20. In 2006, again Antonov and Grigorieva developed Highly Annealed Pyrolytic Graphite (HAPG). Optics made from sheets of HAPG can have mosaic spreads of down to 0.6° and can provide higher spectral resolution than HOPG.^{21–23} The mosaic spread depends on the adhesive forces between substrate and the graphite sheets. The best results were obtained with polished glass molds.²³ If graphite

optics with even lower mosaic spread can be manufactured, and if there is a theoretical limit, is not known.

With view to high resolution X-ray spectroscopy, the most important characteristics of HAPG are: (a) Optics can be produced from HAPG sheets as thick as 20 μm and with mosaic spreads of 0.06°, (b) these sheets can be cold-mounted to substrates of virtually arbitrary shape, (c) an increase in mosaicity or Darwin width due to bending is not reported.

Reflectivity measurements show that kinematical theory²⁴ provides reasonable accuracy for reflectivity calculations of HAPG.²⁵

While the values of mosaicity and reflectivity agree across published experimental results, measured values for the Darwin width are sparse and considerably scatter.²³ We use the value given by Ice and Sparks¹⁵ because it produced the best match of estimates of the spectral resolution and of simulations¹⁶ in comparison with measurements. The manufacturers recommend to use 3.354 Å as a value for the interlayer distance.²⁶

von Hamos spectrometers

To the best of our knowledge, the first who published the use of HOPG in von Hamos geometry were Ice and Sparks almost 30 years ago.¹⁵ In particular, the impact of mosaicity to the spectral resolution is discussed comprehensively. We largely follow the concepts, notions, and equations published in this highly recommendable paper.

Ice and Sparks calculate the spectral broadening by the square sum of a number of contributions. Source size and spatial resolution of the detector are taken directly. The same holds for the Darwin width. The broadening due to mosaicity is modeled with three components, denoted as flat focusing error, penetration error, and roughness error. The flat focusing error stands for the image error due to the crystallites in the surface plane. The penetration error stands for the smearing due to penetration of X-rays. In our calculations, the surface roughness is neglected.

We checked these equations by comparing to more elaborate simulations¹⁶ and experiments. For high resolution optics, where the contribution of the Darwin broadening dominates, they provide good estimates for the spectral resolution.

The crystal related image errors decrease with decreasing mosaicity. With the exception of the flat focusing error and the Darwin broadening, all contributions show a constant broadening in space. Enlarging the distance between the components, i.e., increasing the curvature radius, reduces their size in relation to the wavelength dispersion. In conclusion, a thin crystal (20 μm –40 μm), a low mosaicity ($<0.1^\circ$), and a large bending radius (>100 mm) are required for high spectral resolution. The maximum achievable resolution is determined by the Darwin width like for ideal crystals.

For estimates of the effective solid angle covered by a von Hamos optic, we use the results for peak reflectivity and mosaicity given in the work of Gerlach *et al.*²³ One may also use the work of Zastrau *et al.*²⁵ The effective solid angle of the von Hamos optic is estimated by the product of the integral of the Cauchy profile of the mosaic spread (i.e., the integral reflectivity) times the sagittal angle, the optic spans, times the sine of the Bragg angle. We note that for higher

energies, the profile may be clipped by the finite meridional length of the crystal and the limits of integration must be set accordingly. For the effective solid angle of the entire analyzer, also the quantum efficiency of the detector is taken into account.

We want to conclude with a few final and summarizing remarks on the most important differences between HAPG based von Hamos spectrometers and the ones based on the more frequently used ideal crystals. Ideal crystals are available in various cuts and materials. For the design of spectrometer, frequently crystals are selected which allow for high Bragg angles. High Bragg angles are advantageous with respect to the spectral resolution, solid angle of detection, and instrument size. HAPG can only be used in the 002 plane or in second and higher orders. However, due to the loss of reflectivity already in the second order of reflection, this option is not attractive for laboratory instrumentation. The bending radius and the thickness of the crystal are the two major parameters determining spectral resolution of the optic.

¹O. Lundquist, *Z. Phys.* **33**, 901 (1925).

²D. Coster and M. J. Druyvesteyn, *Z. Phys.* **40**, 765 (1927).

³A. S. Koster and H. Mendel, *J. Phys. Chem. Solids* **31**, 2511–2522 (1970).

⁴K. Tsutsumi, H. Nakamori, and K. Ichikawa, *Phys. Rev. B* **13**, 929–933 (1976).

⁵U. Bergmann and P. Glatzel, *Photosynth. Res.* **102**, 255 (2009).

⁶C. J. Pollock and S. DeBeer, *Acc. Chem. Res.* **48**, 2967 (2015).

⁷C. J. Pollock, M. U. Delgado-Jaime, M. Atanasov, F. Neese, and S. DeBeer, *J. Am. Chem. Soc.* **136**, 9453 (2014).

⁸D. Sokaras, D. Nordlund, T.-C. Weng, R. Alonso-Mori, P. Velikov, D. Wenger, A. Garachtchenko, M. George, V. Borzenets, B. Johnson, Q. Quian, T. Rabedeau, and U. Bergman, *Rev. Sci. Instrum.* **83**, 043112 (2012).

⁹E. Kleymenov, J. A. van Bokhoven, C. David, P. Glatzel, M. Janousch, R. Alonso-Mori, M. Studer, M. Willmann, A. Bergamaschi, B. Henrich, and M. Nachttegaal, *Rev. Sci. Instrum.* **82**, 065107 (2011).

¹⁰H. Hayashi, M. Kawata, R. Takeda, Y. Udagawa, Y. Watanabe, T. Takano, S. Nanao, and N. Kawamura, *J. Electron Spectrosc. Relat. Phenom.* **136**, 191–197 (2004).

¹¹R. Alonso-Mori, J. Kern, D. Sokaras, T.-C. Wenig, D. Nordlund, R. Tran, P. Montanez, J. Delor, V. K. Yachandra, J. Yano, and U. Bergmann, *Rev. Sci. Instrum.* **83**, 073114 (2012).

¹²G. T. Seidler, D. R. Mortenson, A. J. Remesnik, J. I. Pacold, N. A. Ball, N. Barry, M. Styczinski, and O. R. Hoidn, *Rev. Sci. Instrum.* **85**, 113906 (2014).

¹³W. M. Holden, O. R. Hoidn, A. S. Ditter, G. T. Seidler, J. Kas, J. L. Stein, B. M. Cossairt, S. A. Kozimor, J. Guo, Y. Ye, M. A. Marcus, and S. Fakra, *Rev. Sci. Instrum.* **88**, 073904 (2017).

¹⁴L. Anklamm, C. Schlesiger, W. Malzer, D. Grötzsch, M. Neitzel, and B. Kanngießer, *Rev. Sci. Instrum.* **85**, 053110 (2014).

¹⁵G. Ice and C. Sparks, *Nucl. Instrum. Methods Phys. Res., Sect. A* **291**, 110 (1990).

¹⁶C. Schlesiger, L. Anklamm, W. Malzer, R. Gnewkow, and B. Kanngießer, *J. Appl. Crystallogr.* **50**, 1490–1497 (2017).

¹⁷L. C. Jarrott, M. S. Wei, C. McGuffey, F. N. Beg, P. M. Nilson, C. Corce, C. Stoekl, W. Theobald, H. Sawada, R. B. Stephens, P. K. Patel, H. S. McLean, O. L. Landen, S. H. Glenzer, and T. Döppmer, *Rev. Sci. Instrum.* **88**, 043110 (2017).

¹⁸A. Antonov, V. Baryshev, I. Grigorieva, G. Kuipnaov, and N. Shipkov, *Nucl. Instrum. Methods Phys. Res., Sect. A* **308**, 442–446 (1991).

¹⁹I. Grigorieva and A. Antonov, *X-Ray Spectrom.* **32**, 64–68 (2003).

²⁰A. Antonov, I. Grigorieva, B. Kanngießer, V. Arkadiev, and B. Beckhoff, *Handbook of Practical X-Ray Fluorescence Analysis* (Springer, 2006), Vol. 143-157, ISBN: 10 3-540-28603-9.

²¹H. Legall, H. Arkadiev, and A. Bjeoumikhov, *Opt. Express* **14**, 4570–4576 (2006).

²²H. Legall, H. Stiel, H. Schnürer, M. Pagels, B. Kanngießer, M. Müller, B. Beckhoff, I. Grigorieva, A. Antonov, V. Arkadiev, and A. Bjeoumikhov, *J. Appl. Crystallogr.* **42**, 572–579 (2009).

²³M. Gerlach, L. Anklamm, A. Antonov, I. Grigorieva, I. Holfelder, B. Kanngießer, H. Legall, W. Malzer, C. Schlesiger, and B. Beckhoff, *J. Appl. Crystallogr.* **48**, 1381–1390 (2015).

²⁴W. H. Zachariasen, *Theory of X-Ray Diffraction in Crystals* (Dover Publications, 1994).

²⁵U. Zastrau, A. Woldegeorgis, E. Förster, R. Loetzsch, H. Marschner, and I. Uschmann, *J. Instrum.* **8**, P10006 (2013).

²⁶I. Grigorieva and A. Antonov, personal communication (2015).